Università degli Studi di Padova &
Instituto Superior Técnico

DIPARTIMENTO DI INGEGNERIA INDUSTRIALE
Department Of Industrial Engineering

Master of Science Degree in Aerospace Engineering

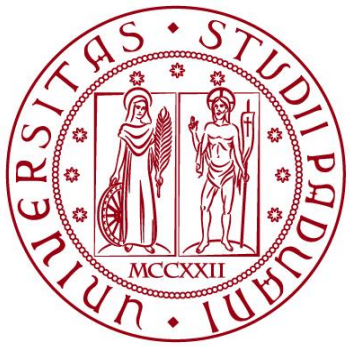

"CFD modelling of Venus aerocapture flow"

Supervisor:
Chiar.mo PROF. FRANCESCO PICANO
Foreigner supervisor:
Chiar.mo PROF. MÁRIO ANTÓNIO PRAZERES LINO DA SILVA

Undergraduate: MARCO PAVANELLO
1220430

ACCADEMIC YEAR 2021-2022

Contents

Abstract

This work aims to study the high-temperature hypersonic flow around a small vehicle for a Venus' atmosphere sampling in order to compute the convective wall heating. The semi-empirical Sutton-Graves correlation were used beyond their limitations for a preliminary estimation for relevant trajectory points where heat fluxes could be maximum. Aerothermal CFD simulations were performed for six trajectory points comprising freestream velocities up to 10.8 km/s. The simulations were performed using the SPARK CFD code, developed and maintained at Instituto de Plasmas e Fusao Nuclear. A comparison between the CFD results and the correlation showed that the Sutton-Graves correlation largely overpredicted the convective heat fluxes, reasserting their inadequacy for this case. An aerothermal analysis at the peak heating point was performed, and the high-temperature flowfield around the vehicle was characterized. Furthermore, different flowfield models were compared and discussed regarding their accuracy and computational cost. This work was made possible by a teamwork with a group of colleagues. Working together on a new Concurrent Design Facility developed at Instituto Superior Tecnico de Lisboa, we were able to share data and help each other to pursue our goal.

Keywords: Aerothermodynamics, Hypersonic, CFD, Venus, Aerocapture

List of Tables

List of Figures

Nomenclature

$\nu'_{i,r}$ stoichiometric coefficients of the reagent i of the forward reaction

$\nu''_{i,r}$ stoichiometric coefficients of the reagent i of the backward reaction

S_i kind of specie

X_i molar concentration of the i^{th} specie

k_{f_r} forward reaction rate coefficient

k_{b_r} backward reaction rate coefficient

$\dot{\omega}_i$ the source term of the mass conservation equation for the i species

c_i mass fraction of the i^{th} specie

M_i molar mass of the i^{th} specie

ε total energy of a particle

e specific internal energy of each species

$(\Delta h_s)_i^o$ effective zero-point energy

R gas constant of the i^{th} specie

ρ density

ψ independent variable

$\boldsymbol{U}$ internal energy of the i^{th} specie

D_i multicomponent diffusion coefficient

p pressure

$[\tau]$ viscous stress tensor

μ gas viscosity coefficient

$[\mathrm{I}]$ identity matrix

E total energy per unit of mass

$\vec{q}_C$ convective heat flux vector

$\vec{q}_D$ diffusive heat flux vector

$\vec{q}_R$ radiative heat flux vector

λ_k thermal conductivity coefficient

T_k temperature associated with the k^{th} energy mode

$\vec{J}_i$ Mass diffusion flux vector of species i^{th}

h_i individual i species' specific enthalpy

$\dot{\Omega}_k$ energy-exchange source term associated with the k^{th} energy mode

ϕ_s scale factor

μ_s species viscosity

Le Lewis number

C_p gas mixture total specific heat at a constant pressure

C_V gas mixture total specific heat at a constant volume

m mass

K coefficient derived as a function of the gas mixture

v velocity

r_n nose radius

$\dot{q}_{conv}$ convective heat flux

$\dot{q}_{rad}$ radiative heat flux

K_n Knudsen number

d hard-shell diameter

l spacific length

Re_w Reynolds number at the wall

Acronyms

CFD Computational Fluid Dynamics

CDF Concurrent Design Facility

CFL Courant–Friedrichs–Lewy

DSMC Direct Simulation Monte Carlo

GMAT General Mission Analysis Tool

IPFN Instituto de Plasmas e Fusao Nuclear

IST Instituto Superior Tecnico

NASA National Aeronautics and Space Administration

SPARK Software Package for Aerothermodynamics, Radiation and Kinetics

TPS Thermal Protection System

MATLAB Matrix Laboratory

Chapter 1

Introduction

A new Concurrent Design Facility (CDF), dubbed LAICA, is under development at the main campus of Alameda, downtown Lisbon. Concurrent Design brings a structured approach to assessment studies and pre-Phases A mission development. In the context of the renewal of the pedagogical offer and increased interest in multidisciplinary teaching modules across IST departments and research units, the CDF brings a valuable tool to faculty and researchers, allowing for experts in different disciplines to interact towards the common goal of concurrently designing complex and innovative systems [1]. The students contributed to the CDF engineering tools and database in order to develop their MSc Diploma thesis.
One of the first work developed in this room was a mission named "Venus Atmosphere Sample Analysis (VASA) Probe" that consists in a Venus' atmosphere measuring and onboard analysing, made with an aerocapture. A team of students and a faculty, acting as Team Leader, supported by the CDF developer, shared responsibilities for each planned study.
More specifically, this thesis will provide some CFD simulations in order to evaluate the heat fluxes occurring during the aerocapture. The input of these simulations were the upstream conditions supplied by one member of the CDF, the mission analyst. The heat fluxes obtained through the CFD simulations will be the output, and comparing them with some previous previous models, they will be used by the TPS analyst to model the thermal protection shield of the spacecraft.

1.1 Scientific Motivation

Venus, Earth's evil sister, has always fascinated humans and, among them, the scientists as well. However, our knowledge of the nearest and most similar planet in size and mass is poor, and many unknowns are still present today. Even if there are similarities between the planets, one has oceans of liquid water and hosts a multitude of life forms, while the other is often described as a hellscape. This is due to the fact that the two planets evolved in a very different way: Venus' atmosphere is dominated by CO_2 (96.5% by volume) and N_2 (3.5%), with smaller amounts of noble gases (He, Ne, Ar, Kr, Xe) and chemically reactive trace gases (SO_2, H_2O, CO, OCS, H_2S, HCl, SO, HF, and elemental sulphur vapour), that results in an extreme greenhouse effect, leading to an average surface temperature of 464 °C [2] [3]. The dense atmosphere also results in a surface pressure of $\sim$ 93 bar. A global opaque cloud layer covers the surface from the sunlight at visible wavelengths and vertically extends from $\sim$ 47.5 to $\sim$ 70 km, composed mainly by liquid sulphuric acid (H_2SO_4) and water [4]. High values of Deuterium/Hydrogen (D/H) ratio were found, suggesting a possible loss of atmospheric water. Highly variable atmospheric conditions are present through this layer that also comprises a possible habitable zone [2].
It is known how the solar system has formed, and which are the main steps that brought the small particles around our proto-Sun to become the planets we know today, however a lot of uncertainties are present on the various mechanisms going one during these steps, and their influence on the evolution of the planets. Since its beginning, space exploration has helped the

scientific community to answer many of these questions and the exploration of extra-terrestrial planets has been extremely useful to understand the histories of evolution of the single bodies and of the solar system itself. Venus' exploration has however always been making engineers' life difficult, due to the harsh environment it presents. Nevertheless, it became the first planet to be explored, both from orbit, with Mariner 2 flyby, and from the surface, with Venera 7. Indeed, the Venera program of USSR provided a huge quantity of information of the planet, that allowed to understand better the complex atmosphere surrounding the planet and responsible for the climate near the surface. However, after the end of the program, just orbiters or flybys were sent to the planet unable, given their nature and the particularities of the atmosphere, to provide comprehensive information. In order to answer most of the questions left unanswered, samples of the atmosphere and their analysis with modern instruments are needed, the sampling of the upper atmosphere to collect and analyse in-situ noble gases and their isotopic fractionations, of crucial importance in the study of planetary evolution as they keep a trace of the planet's history, not reacting with the surface or other gases. Precise measurements are needed to discriminate among different scenarios to improve our understanding of the Solar system's early evolution and of the mechanisms that led Venus to its present state thus helping to resolve unknowns on the terrestrial evolution. The resistance of noble gases to chemical interactions results in very weak coupling to electromagnetic interactions and therefore in a weak spectral signature, excluding remote sensing and making a sample analysis necessary for their identification.
Beside the interest in planetary formation and atmosphere evolution, many scientific questions are still open regarding Venus' atmosphere. One of the open questions regarding Venus is why the planet rotates so slowly and why its atmosphere rotates 40 to 60 times faster than it: the so-called superrotation.
The atmosphere of Venus has many complex chemistry processes that control its enormous atmosphere; three major cycles have been identified: the carbon dioxide cycle, the sulphur oxidation and the poly-sulphur one. The first two have been observed directly, while the third one is still speculative [5].
Another important question is if the planet is habitable or not. The poisonous atmosphere of CO_2, the extreme temperatures and pressures and the corrosive amounts of sulphuric acid make Venus not suitable for life on its surface. The presence of phosphine had suggested this question recently. According to new studies, the phosphine is unexplained through steady-state chemistry or photochemical pathways, leading to no currently known abiotic production routes in Venus' atmosphere, clouds, surface and subsurface, or from lightning, volcanic or meteoritic delivery. It could however originate from unknown photochemistry or geochemistry, but this question is still open [6].

1.2 Atmospheric Entry Overview

Hypersonic flow is usually defined as having free streams with a Mach number greater than five. In the hypersonic regime there are strong compressibility effects, hence the formation of a high-temperature shock wave. Consequently, the flow experiences the rise of high-temperature effects such as dissociation, ionization, thermal and chemical non-equilibrium, among others [7].
Typical Earth re-entry velocities are in the range of 7.7 km/s from orbital trajectories and 14 km/s for super orbital hyperbolic trajectories. As the vehicle's speed is higher than that of the sound, a detached strong shock wave builds up in front of the body, converting kinetic energy into thermal energy that is dissipated to the moving flow [8].

The detached shock is created due to the blunt nose of the entry vehicle, allowing a standoff distance between the high-temperature shock wave and the vehicle, forming a shock layer between the two, which promotes endothermic reactions that will retire some of the energy of the flow before hitting the vehicle's surface. The temperatures in the shock layer are high enough to excite the internal modes of the particles in the flow, making them accessible reservoirs for storing thermal energy. Molecules will store energy until inter-nuclear bounds are overcome and dissociation takes place. Similarly, bound electrons are brought to excited levels and can even leave their parent particle, leading to ionization.
However, this also means that the vehicle will be immersed in a hot layer of plasma, and nevertheless subjected to extreme heating. The heating process occurs through two mechanisms: convective heating and radiative heating. Convective heating occurs by direct interaction and collisions between the energetic particles of the flow and the vehicle's surface. It is composed of a conduction component determined by the temperature gradient, and a diffusive component determined by the mole fraction gradient. Radiative heating occurs due to the absorption of radiation emitted by the surrounding particles in the shock layer. Depending on the entry speed, one of these two mechanisms can be dominant over the other. Furthermore, the relevance of each mechanism is also a function of the capsule geometry, implying that a capsule with a larger nose radius will promote a thicker shock layer, increasing the amount of radiation it absorbs [7] [9].

This work considers the entry of a small vehicle with super orbital velocity on the atmosphere of Venus. Among other phenomena, this ionized plasma will create a current of ions and electrons around the capsule, blocking radio communications and leading to the so-called communications blackout, a critical challenge for mission control. For hypersonic flow, the time needed for vibrational relaxation and chemical reactions may be similar to, or higher than, the characteristic flow time. This means that some regions of the flow will be in non-equilibrium, i.e., the number of collisions of particles is insufficient to complete the chemical reactions and energy exchange. Furthermore, the non-equilibrium phenomenon is more prevalent at higher altitudes, where particle density is lower. Due to the strong favourable pressure gradients and low Reynolds number at the stagnation point, the laminar-turbulent transition is delayed, and the flow in the forebody region is assumed to be laminar. The maximum heat fluxes, take place at around 95.3 km altitude, where the flow is commonly assumed to be continuum and can be mathematically formulated throughout finite volume methods and Navier-Stokes equations. For higher altitudes, where the air is significantly more rarefied, the flow can no longer be considered continuum, and statistical methods such as Direct Simulation Monte Carlo (DSMC) must be employed 8. Figure 1.1 describes some of the phenomena occurring in the flowfield along the stagnation line of a vehicle with non-ablative TPS (Thermal Protecting System) during an Earth atmospheric reentry as an example. As the particles approach the shock wave, they experience radiation emitted from the hot shock layer, leading to precursor phenomena of and pre-dissociation [10].
Across the shock wave, most of the kinetic energy of the particles is converted into translational energy as they hit the dense shock wave. Inter-particle collisions also lead to the molecules' rotational, vibrational, and electronic excitation.
Provided sufficient energy, the molecules quickly build up large amounts of vibrational energy, their internuclear bounds are broken and dissociation occurs. Electronic excitation through further collisions in the pool of particles excites the bound electrons to elevated states and even makes them leave the parent nuclei, leading to ionization.

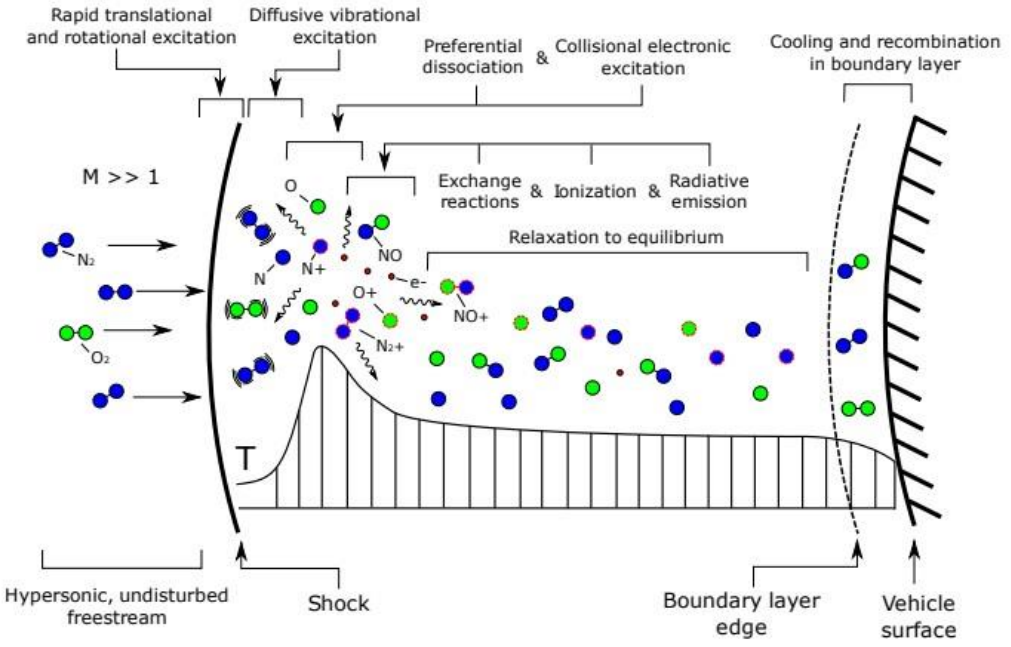

Fig 1.1: *Shock layer high-temperature effects in Earth's atmosphere.* [11]

Afterwards, as the charged particles decay to less energetic levels, the gas will radiate electromagnetic energy. Sufficiently downstream of the shock, and after many collisions have occurred, a thermal equilibrium region is eventually established. As the plasma hits the high-density boundary layer, heat convects to the vehicle surface and the gas temperature drops, allowing some recombination to occur.
In order to assess the heat transfer to the vehicle and design a suitable TPS, the multi-physics and chemical phenomena described above must be properly modelled. The accurate modelling of hypersonic flow involves the numerical solution of a suitable set of governing equations – the compressible Navier Stokes equations – which are further discussed in Chapter 2.

1.3 Objectives of this work

The purpose of this thesis will be to:

- Evaluate the convective heat fluxes for each trajectory key points.
- Test two different chemistry for the flow: one that assume a 5-species flow, and one with 10-species.
- Provide a first estimate of the heat fluxes for the next phase of the design.

In order to accomplish these objectives, CFD simulations will be performed. The Wilke transport model will be considered for the simulations, and, since we are going to assume thermal equilibrium conditions, a one-temperature model will be used. To reach these tasks the SPARK code is used, with the help of an Excel spread sheet to take account of different simulations tested.

1.4 Thesis outline

This thesis is divided in five main chapters. The current Chapter 1 presents the challenges of the hypersonic flight and the motivation that brought the development of this thesis.

Chapter 2 presents the mathematical formulation and the physical models for high-temperature hypersonic flows, including fluid dynamics, thermodynamics, chemical-kinetics, and transport properties models.
Chapter 3 presents the numerical implementation of the physical models. It sets up all the parameters for the CFD simulations, including the computational domain and the upstream boundary conditions, which are dependent on the vehicle and trajectory design. The CFD numerical solver and simulation strategy is also presented in this chapter.
Chapter 4 presents the numerical results of the CFD simulations, where the wall heat fluxes and the impact of the flowfield models are discussed.
Finally, Chapter 5 presents the main achievements of this work and provides some ideas and recommendations for future work.

Chapter 2

Mathematical Formulation

In order to perform a CFD simulation of an atmospheric entry, we need to discuss some theoretical formulation to properly face the problem. Discussing the governing equations and the physics of hypersonic flow is the first step required. To accurately develop a model for a Venus atmospheric entry, we must take account of different physical phenomena that occurs when we fly at very high Mach number:

- *Thin Shock Layer*, that is as Mach number increases, the density of the fluid between the shock wave and the body becomes thinner.
- *The Entropy layer*, that causes analytical problems when we want to do a standard boundary-layer calculation on the surface.
- *Viscous Interaction*, that can have a tremendous impact on the surface pressure distribution, lift and stability of the vehicle.
- *High-Temperature effects,* caused by the extreme viscous dissipation. The vibrational excitation and chemical reactions take place very rapidly compared to the time it takes to the fluid to move through the flow field, we have vibrational and chemical equilibrium. But if it doesn't happen, we have a nonequilibrium flow, which is more difficult to analyse. High temperature effects are the most dominant aspect of the hypersonic aerodynamic.
- *Low density flow*, that implies that a vehicle experiences different regimes for the atmosphere: from a free molecular regime, at the upper part of the atmosphere, through a transition regime and to the continuum regime for the denser atmosphere. [7]

Throughout this work a model of different species will be used to describe Venus's ionized atmosphere gas, consisting of the following species:

$$CO_2,\ O_2,\ CO,\ C,\ O,\ O_2^+,\ CO^+,\ C^+,\ O^+,\ e^-$$

As already mentioned, we neglect the little amount of N_2 in the Venus atmosphere since it doesn't give any significant impact on the results. To accurately model this type of flow we are considering the flow in a state of chemical non-equilibrium. Moreover, to characterize this complex environment, we will use the conservation equations applied to the conserved quantities of the flow, under the assumption there is continuum flow. These equations consider the non-equilibrium state and depend on chemical-kinetic and transport model.

2.1 Non-equilibrium Reacting Flow

2.1.1 Chemical non-equilibrium

When the gas doesn't experience any spontaneous changes in its chemical composition, that is when all chemical reactions are in balance, the composition of the system is uniquely described by two thermodynamic variables. However, when the fluid passes through the shock, pressure and temperature rapidly increase with a change in the chemical equilibrium property of it. The low characteristic time of the hypersonic flows doesn't allow the necessary collisions to take place and, therefore, there is a region inside the shock layer where chemical equilibrium is not reached, even in steady state flow condition.
Due to chemical non-equilibrium, the gas cannot be modelled only as function of the gas state variables and chemical-kinetic models need to be applied. This requires finding the solution of one mass conservation equation per chemical species considered. In order to obtain the expression for the source term in the mass conservation equation, proper modelling of the reactions taking place must be achieved. The general chemical reaction is given as:

$$\nu'_{1,r}S_1 + \nu'_{2,r}S_2 + \cdots + \nu'_{n,r}S_n \leftrightharpoons \nu''_{1,r}S_1 + \nu''_{2,r}S_2 + \cdots + \nu''_{n,r}S_n \tag{2.1}$$

where $\nu'_{i,r}$ and $\nu''_{i,r}$ represent the stoichiometric coefficients of the reagent i of the forward and backward *r-th* reaction. S_i are different kind of species [12]. The net rate of formation of species i can be given by:

$$\frac{d[X_i]}{dt} = \sum_r (\nu''_{ir} - \nu'_{ir})[k_{f_r} \prod [X_i]^{\nu'_{ir}} - k_{b_r} \prod [X_i]^{\nu''_{ir}}] \tag{2.2}$$

Where $[X_i]$ represents the molar concentration of the i species in the reaction r. Equation (2.2) expresses the net rate for production of the i^{th} species through reaction r. k_{f_r} and k_{b_r} are respectively the forward reaction rate coefficient and the backward reaction rate coefficient which are given by the modified Arrhenius equation for chemical kinetics [13]:

$$k_{f_r} = A_f T^{B_f} e^{(-\frac{C_{fr}}{T})} \tag{2.3}$$

$$k_{b_r} = A_b T^{B_b} e^{(-\frac{C_{fb}}{T})} \tag{2.4}$$

The rate of creation or consumption of each chemical species is $\dot{\omega}_i$, the source term in the species continuity equation (2.8), computed as:

$$\dot{\omega}_i = M_i \frac{d[X_i]}{dt} = M_i \sum_r (\nu''_{ir} - \nu'_{ir})[k_{f_r} \prod [X_i]^{\nu'_{ir}} - k_{b_r} \prod [X_i]^{\nu''_{ir}}] \tag{2.5}$$

Which represents the source term of the mass conservation equation described in the following sub-chapter. M_i represents the molar mass of the i^{th} species [14] [15].

2.1.2 Thermal non-equilibrium

At orbital hypersonic speeds, as the flow crosses the shock wave, its great amount of kinetic energy is converted into thermal energy as the internal degrees of freedom of the gas are excited. These degrees of freedom are reservoirs of thermal energy divided into four main thermal energy modes, as represented in Figure 2.1: translational, rotational, vibrational and electronic excitation modes. Each of these modes determine the energy of the particles of the plasma, which is made of atoms, molecules, ions and electrons. Depending on the type of particle, its energy content is distributed in different modes. Molecules have all four the

thermal energies, while atoms only have translational and electronic forms of energy. The sources of energy of the translational, rotational and vibrational modes are the translational kinetic energy of the centre of mass of the particle, the rotation of the molecule about the three orthogonal axes in space and vibration of the atoms with respect to an equilibrium location within the molecule, respectively. The energy associated to the electronic mode is related to the motion of electrons about the nucleus of atoms and it has two sources: kinetic energy, as a result of the motion of electrons and potential energy, due to the electrons' location in an electromagnetic force field. Free electrons only possess translational kinetic energy.

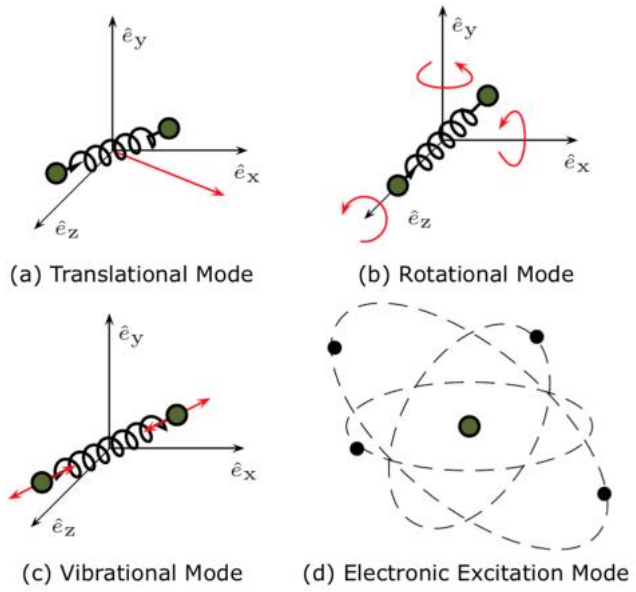

Fig 2.1: *different energy modes*.

The motion of the molecule can be resolved into three components (x, y, z), each one contributing to the total kinetic energy. Thus, it is said to have three translational thermal degrees of freedom. Similarly, a molecule rotates about the three orthogonal axes in space. The energy associated to this rotational velocity and to the molecule's moment of inertia contributes to the total rotational kinetic energy in the three different ways, associated to each one of the axes. The moment of inertia about the internuclear axis (y axis in Fig 2.1) is negligible, so it is said that has only two rotational thermal degrees of freedom. Furthermore, the atoms of a diatomic molecule vibrate with respect to an equilibrium position. This mode adds one or more degrees of freedom depending on whether the molecule is diatomic or polyatomic. The orbital motion of the electron around the nucleus adds yet another energy storage mode. So, the total energy of a particle can be given by the following expression:

$$\varepsilon = \varepsilon_{tra} + \varepsilon_{rot} + \varepsilon_{vib} + \varepsilon_{exc} + \varepsilon_0 \tag{2.6}$$

Where each of the terms on the right of the equal represent an energy mode, and the ε_0 corresponds to the zero-point energy, a fixed quantity for a given specie. From a macroscopic point of view, the specific internal energy of each species, will be:

$$e_i = e_{tra,i} + e_{rot,i} + e_{vib,i} + e_{exc,i} + (\Delta h_s)_i^o \tag{2.7}$$

Where this time *e* corresponds to the specific internal energy of each mode and $(\Delta h_s)_i^o$ corresponds to the effective zero-point energy. The terms at the right of the equal are:

$$\begin{cases} e_{tra,i} = \frac{3}{2} R_i T \\ e_{rot,i} = R_i T \\ e_{vib,i} = e_{vib,i} \\ e_{el,i} = e_{el,i} \end{cases} \quad (2.8)$$

Where $e_{vib,i}$ is:

$$e_{vib,i} = \frac{h\nu_i/kT}{(e^{h\nu_i/kT}-1)} R_i T \quad (2.9)$$

If we assume local thermodynamic equilibrium.
If vibrational non-equilibrium is present, then $e_{vib,i}$ is given by:

$$\frac{D(c_i e_{vib})}{Dt} + \frac{1}{\rho} \nabla \cdot \left(\rho_i U_i e_{vib,i}\right) = \frac{c_i}{\tau} \left(e_{vib,i}^{eq} - e_{vib,i}\right) \quad (2.10)$$

In a low-density regime, the energy exchange is slow when compared to the velocity of the flow, so at high altitudes, the number of collisions required to achieve thermal equilibrium does not occur. In fact, the relaxation time of the energy exchanges are larger than the characteristic time of the flow, which is in the domain of thermal non-equilibrium.
When it is assumed thermal equilibrium, all the four energy modes have the same temperature. Some regions of the flow could be described by this approach, while others, like the region behind a strong shock wave, may not. So, in this case, a multi-temperature model should be considered. When this multi-temperature approach is considered, the global internal energy can be given by the sum of individual species energy associated with each thermal mode:

$$e = \sum_i c_i e_i \quad (2.11)$$

Where c_i represents the mass fraction and e_i is the specific internal energy of the i^{th} species. And e represent the global internal energy of the system [16].

2.1.3 Two-Temperatures model

The two-temperature model is a good compromise between the too simple one-temperature model and the more complex three-temperature model. What justify the usage of this model is the rapid energy transfer between the translational mode of free electrons and the vibrational mode and the rapid equilibration of the low-lying electronic states of heavy particles with the ground electronic state at the electronic temperature. This model is the one used for SPARK to model a non-equilibrium flow using two different temperatures:

- $T_{tra\text{-}rot}$: the translational-rotational global temperature, common to the translational mode of heavy species, and the rotational mode of molecules.
- $T_{vib\text{-}exc}$: this temperature is used to characterize the molecular vibrational, electron translational and electronic excitation energy modes.

The evaluations of specific heats and enthalpies are much simpler in the two-temperature model. The fact that the translational and rotational energy modes are assumed to be fully excited implies that the heat capacities for these modes are independent of temperature.

Although the two-temperature approximation may not be valid in the viscous boundary layer region at the wall, this formulation allows a more tractable formulation in terms of computation of reacting flows in thermal non-equilibrium.
More complex models can be used in case of high-temperature problems. However, the number of models that can be defined are limited to their physical relevance, to the increased computational effort and to the relaxation models available.
The two-temperature model choice is based on the knowledge that it is legitimate to be valid for an atmospheric entry, and on the fact that for the purpose of simulating flow fields over hypersonic it accurately predicts the aerodynamic coefficients and radiative and convective heating on the surface of the probe [17].
Since the focus here is the convective heating at the wall, the simulation was simplified, considering solely a single-temperature model. This means that the shock-layer will not be as accurately reproduced as with a two-temperature model (T,T_v), however this will have no bearing in the boundary layer region, since for this high velocity regimes, there is a quasi-steady-state region between the shock and boundary layers, where thermodynamic properties (translation and internal temperatures) have enough time to equilibrate [18].

2.2 Conservation Equations

The complete system of partial differential equations that governs non-equilibrium viscous chemically reacting flow corresponds to an extension of the traditional Navier-Stokes conservation equations. They are applied to the mass of species (chemical non-equilibrium), momentum, total energy and thermal energy (thermal non-equilibrium) variables in which continuum flow is assumed, and intermolecular forces, present at a microscopic level, are neglected. It is important to state that the continuity and the momentum are purely mechanical in nature, so they are not affected by any chemical reactions. It is a system of partial differential equations, in which ψ is the independent variable:

$$\frac{\partial(\rho\psi)}{\partial t} + \boldsymbol{\nabla}\cdot(\rho\psi\boldsymbol{U}) = \boldsymbol{\nabla}\cdot\boldsymbol{J}_{\psi} + S_{\psi} \tag{2.12}$$

Where:

- $\frac{\partial(\rho\psi)}{\partial t}$ is the transient term,
- $\boldsymbol{\nabla}\cdot(\rho\psi\boldsymbol{U})$ is the convective term,
- $\boldsymbol{\nabla}\cdot\boldsymbol{J}_{\psi}$ is the diffusive term,
- S_{ψ} is the source term.

2.2.1 Species Conservation

The following equation represents the mass conservation for each chemical species. It considers the production of each chemical species represented by the term $\dot{\omega}_i$.

$$\frac{\partial(\rho c_i)}{\partial t} + \boldsymbol{\nabla}\cdot(\rho c_i\boldsymbol{U}) = -\vec{\nabla}\cdot\vec{J}_i + \dot{\omega}_i \tag{2.13}$$

Where ρ is the total density (that is the summation of the density of the species i), c_i is the mass fraction of the i^{th} species and $\dot{\omega}_i$ is the mass production rate of species *i* represented by the equation (2.3). Considering a control volume in which a gradient in mass fraction of species *i* exists, $\vec{J}_i$ is the mass flux of species *i*, given approximately by the Fick's Law as:

$$\vec{J}_i \equiv \rho_i \vec{u}_i = -\rho D_i \vec{\nabla} c_i \tag{2.14}$$

Where $\vec{u}_i$ is the velocity of the i^{th} species, D_i is the multicomponent diffusion coefficient for species i through the mixture and ρ_i is the density of the single species.
This equation implies that the total mass of the mixture remains constant, although the total mass of a given species may change.

2.2.2 Mixture Momentum Conservation

The following equation represents the conservation of the momentum, which is a result of Newton's second law applied to the motion of fluids:

$$\frac{\partial(\rho\vec{u})}{\partial t} + \vec{\nabla} \cdot (\rho\vec{u} \otimes \vec{u}) = \vec{\nabla} \cdot [\tau] - \vec{\nabla} p \tag{2.15}$$

Where p is the pressure and $[\tau]$ is the viscous stress tensor that is represented by the following equation:

$$[\tau] = \mu\left(\vec{\nabla}\vec{u} + \left(\vec{\nabla}\vec{u}\right)^T\right) - \frac{2}{3}\mu(\vec{\nabla} \cdot \vec{u})[\mathrm{I}] \tag{2.16}$$

Where the Stoke's hypothesis for the fluid is assumed for a Newtonian stress-strain rate relation is assumed, μ is the gas viscosity coefficient and $[\mathrm{I}]$ is the identity matrix. It is important to state that this formulation assumes that the gas moves with a global velocity $\vec{u}$. This is a practical assumption, because the computational effort is compared to a more realistic scenario, in which one vectorial momentum equation for each species is considered. Moreover, this approximation is valid when the constituent species have similar mass and there is no ionisation in it.

2.2.3 Total Energy Conservation

It's important to consider the total energy conservation of the system by the following equation:

$$\frac{\partial(\rho E)}{\partial t} + \vec{\nabla} \cdot (\rho E\vec{u}) = \vec{\nabla} \cdot (-\vec{q} - (p\vec{u}) + (\vec{u} \cdot [\tau])) \tag{2.17}$$

Where E is the total energy per unit of mass, and $\vec{q}$ is the heat flux vector composed by the following terms:

$$\vec{q} = \vec{q}_C + \vec{q}_D + \vec{q}_R = \sum_{\boldsymbol{k}} \vec{q}_{C_k} + \sum_{\boldsymbol{i}} \vec{J}_i h_i + \vec{q}_R \tag{2.18}$$

Where h_i is the i^{th} species enthalpy. The terms at the right of the equal accounts for thermal conduction, transport of energy by diffusion, radiative energy emitted or absorbed by a fluid element. The Fourier's Law of heat conduction is used to determine the conduction of heat fluxes $\vec{q}_{C_k}$ for each thermal energy mode as:

$$\vec{q}_{C_k} = -\lambda_k \vec{\nabla} T_k \tag{2.19}$$

Where λ_k and T_k are the thermal conductivity coefficient and temperature associated with the k^{th} energy mode. $\vec{q}_R$ is the radiative heat flux vector.

2.2.4 Non-equilibrium Thermal Energy Conservation

To accurately model flow in thermal non-equilibrium, an additional conservation equation for the non-equilibrium temperature is required. Considering the two-temperature model, there is only one non-equilibrium thermal energy conservation equation referred to the vibrational-electronic energy conservation, whereas for the three-temperature model, in which the electronic excitation mode is in equilibrium with the free electrons' translation, is:

$$\frac{\partial \rho e_k}{\partial t} + \vec{\nabla} \cdot (\rho \vec{u} h_k) = \vec{\nabla} \cdot \left(\vec{q}_{C_k} - \sum_i \vec{J}_i h_{i,k} + \vec{q}_R \right) + \dot{\Omega}_k \qquad (2.20)$$

Where e_k is the specific internal energy of the k^{th} thermal energy mode and $\dot{\Omega}_k$ is the energy-exchange source term associated with the k^{th} energy mode [7].

2.3 Transport Properties

Diffusion, viscosity and thermal conduction are the physical phenomena that become very important at high temperature and chemically reacting flow. These fluxes are fundamental for modelling the transport of mass, momentum and energy through the gas, respectively.

	Dissipative fluxes		Transport coefficient		Gradient		Model
Mass diffusion	$\vec{J}_i$	[kgm^{-2}s^{-1}]	D_i	[m^{2}s^{-1}]	$\vec{\nabla} c_i$	[m^{-1}]	Fick's Law
Viscosity	$[\tau]$	[Nm^{-2}]	μ	[kgm^{-1}s^{-1}]	$\vec{\nabla}\vec{u}$		Newtonian Fluid
Thermal conduction	$\vec{q}_{C_k}$	[Jm^{-2}s^{-1}]	λ_k	[Jm^{-1}s^{-1}K^{-1}]	$\vec{\nabla} T_k$	[Km^{-1}]	Fourier's Law

Tab 2.1*: List of dissipative fluxes and related transport coefficients, gradients and models in SI units.*

To determine the flow transport coefficients is required to know the behaviour of the gas towards concentration, velocity and temperature gradients. Besides the continuously changing chemistry, temperature and pressure in this type of flow, which requires the knowledge of the altering transport properties, the possibility of ionisation introduces ambipolar diffusion, which also changes the gas mixture transport properties. SPARK can compute these properties in real-time during a CFD simulation, using two different models based on mixing rules: the Wilke/Blottner/Eucken and the Gupta-Yos/CCS models. These simplified models substitute the classical and computationally expensive Chapman-Enskog solution of the Boltzmann equation.

2.3.1 Transport Models

Wilke/Blottner/Eucken Model

Wilke's model for gas mixture viscosities was developed in 1950 through the application of the kinetic theory to the first order Chapman-Enskog relation. It is a mixing rule which assumes that all interactions between any particles present the same cross-section. It provides the transport coefficients for the chemical species. However, in order to couple this model to a

state-resolved kinetic scheme, it is considered that the transport coefficient contribution of each sub-species *v/w* is equal to the transport coefficient contribution of the corresponding chemical species *s/r* [16].
The gas mixture viscosity μ and the thermal conductivity λ_k for each global thermal energy mode are obtained using the following mixing rules:

$$\mu = \sum_v \frac{x_v \mu_s}{\phi_s} \qquad ; \qquad \lambda_k = \sum_v \frac{x_v \lambda_{k,s}}{\phi_s} \tag{2.21}$$

Where x_v is the molar fraction of each sub-species v and μ_s represents the species individual viscosities. ϕ_s is a scale factor defined in the following way [19]:

$$\phi_s = \frac{\sum_r [1 + \sqrt{\frac{\mu_s}{\mu_r}} (\frac{M_r}{M_s})^{\frac{1}{4}}]}{\sqrt{8(1 + \frac{M_r}{M_s})}} \tag{2.22}$$

Where M_s and M_r represents each species molar mass. The species viscosities μ_s are obtained through curve fits.

$$\mu_s(T_{tra,s}) = 0.1 \cdot \exp\left((A_s \ln T_{tra,s} + B_s) \ln T_{tra,s} + C_s\right) \tag{2.23}$$

Where A_s, B_s and C_s are curve fitted coefficients for each species.
The thermal conductivity associated to each one of the thermal energy modes – $\lambda_{tra,s}$, $\lambda_{vib,s}$, $\lambda_{rot,s}$ and $\lambda_{el,s}$ – can be obtained using Eucken's relation:

$$\lambda_{tra,s} = \frac{5}{2} \mu_s C_{Vtra,s} \qquad ; \qquad \lambda_{k \neq tra,s} = \mu_s C_{Vk,s} \tag{2.24}$$

Where $C_{Vtra,s}$ is the specific heat at a constant volume of species s in the translational energy mode.
The species mass diffusion coefficient is given by a single binary coefficient D assuming a constant Lewis number, Le = 1.2:

$$D_s = D = \frac{Le\lambda}{\rho C_p} \tag{2.25}$$

Where C_p represents the gas mixture total specific heat at a constant pressure and λ represents the total thermal conductivity of the gas mixture. The Lewis number Le defines the ratio of the energy transport due to mass diffusion relative to that due to thermal conduction [16].

Gupta-Yos/Collision Cross-Section

The Gupta-Yos model is an approximate mixing rule that provides the transport coefficients for the chemical species. This model is a simplified form of the classical Chapman-Enskog solution for the Boltzmann equation system. It is assumed that to be more accurate than the Wilke's Model, since it accounts for the true nature of the viscosity collision integrals by considering the corresponding collision cross-sections. However, it requires an accurate collision integral data for each species pair in the gas mixture, thus it is not possible to implement this model if there is no sufficient data available.
In order to couple this model to a state-resolved kinetic scheme, it was considered that the transport coefficients of each sub-species v/w were equal to the transport coefficients of the corresponding chemical species s/r.

The collision integrals $\Delta_{sr}^{(1)}$ and $\Delta_{sr}^{(2)}$, between species s and r, are defined as a function of the control Temperature T_c:

$$\Delta_{sr}^{(1)} = \frac{8}{3}\left[\frac{2M_sM_r}{\pi R_u T_c(M_s+M_r)}\right]^{\frac{1}{2}} \pi\bar{\Omega}_{sr}^{(1,1)}(T_c) \times 10^{20} \tag{2.26}$$

$$\Delta_{sr}^{(2)} = \frac{16}{5}\left[\frac{2M_sM_r}{\pi R_u T_c(M_s+M_r)}\right]^{\frac{1}{2}} \pi\bar{\Omega}_{sr}^{(2,2)}(T_c) \times 10^{20} \tag{2.27}$$

Where $\pi\bar{\Omega}_{sr}^{(1,1)}$ and $\pi\bar{\Omega}_{sr}^{(2,2)}$ represent weighted averages of the cross-sections, which are evaluated as curve fits to the tabular data generated. The controlling temperature T_c depends on the particles colliding. It is referred to the heavy-species translational temperature $T_{tra,h}$, except if the collision involves electrons, in which case the electrons temperature would be $T_{el}=T_{tra,el}$.

For calculation purposes, the gas mixture viscosity will be:

$$\mu = \sum_v \frac{m_s x_v}{\sum_w x_w \Delta_{sr}^{(2)}} \tag{2.28}$$

Where m_s is the s-th species mass. Will be defined the translational mode of heavy species (λ_{tra}) and electrons (λ_e) as it follows:

$$\lambda_{tra} = \frac{15}{4}k_B \sum_{v\neq e} \frac{x_v}{\sum_w \alpha_{s,r} x_w \Delta_{sr}^{(2)}(T_{tra})} \quad ; \quad \lambda_e = \frac{15}{4}k_B \sum_{v\neq e} \frac{x_e}{\sum_w \alpha_{e,r} x_w \Delta_{er}^{(2)}(T_{vib})} \tag{2.29}$$

Where k_B is the Boltzmann constant and $\alpha_{s,r}$ is given by:

$$\alpha_{s,r} = 1 + \frac{[1-M_s/M_r][0.45-2.54(M_s/M_r]}{[1+(M_s/M_r)]^2} \tag{2.30}$$

The global thermal conductivities associated with the rest of the heavy species energy modes will be defined as follow:

$$\lambda_{rot} = \sum_{v=m} \frac{x_v m_s C_{V_{rot,s}}}{\sum_w x_w \Delta_{sr}^{(1)}} \quad ; \quad \lambda_{vib} = \sum_{v=m} \frac{x_v m_s C_{V_{vib,s}}}{\sum_w x_w \Delta_{sr}^{(1)}} \quad ; \quad \lambda_{exc} = \sum_{v=m} \frac{x_v m_s C_{V_{exc,s}}}{\sum_w x_w \Delta_{sr}^{(1)}} \tag{2.31}$$

Where m denotes a molecular species. In thermal equilibrium, the total thermal conductivity λ is determined by the following equation:

$$\lambda = \lambda_{tra} + \lambda_e + \lambda_{rot} + \lambda_{vib} + \lambda_{exc} \tag{2.32}$$

In thermal non-equilibrium, the thermal conductivity associated with each thermal energy mode is calculated considering the individual contribution of each species to that same mode, according to the multi-temperature model taken as a reference.

The mass diffusion coefficient D_{sr} defines the diffusion velocity of each species relative to the different species and can be as expressed as:

$$D_{sr} = \frac{k_B T_c}{p\Delta_{sr}^{(1)}} \tag{2.33}$$

The effective diffusion coefficient is determined by considering the multi-component mixture as a binary mixture consisting of specie s and a composite specie that represents the contribution of the remaining species. It is given by the following equation:

$$D_s = \frac{1 - x_s}{\sum_{r \neq s} \frac{x_r}{D_{sr}}} \tag{2.34}$$

For a single specie mixture, its properties are determined by the following equations:

$$\mu_s = \frac{5}{16} \frac{\sqrt{\pi m_s k_B T_c}}{\pi \bar{\Omega}_{sr}^{(2,2)}} 10^{20} \tag{2.35}$$

$$\lambda_{tra,s} = \frac{75}{64} k_B \frac{\sqrt{\pi k_B \, T_c / m_s}}{\pi \bar{\Omega}_{sr}^{(2,2)}} 10^{20} \tag{2.36}$$

$$\lambda_{rot,s=m} = \frac{8}{3} k_B C_{V_{rot,s}} \frac{\sqrt{\pi k_B T_c m_s}}{\pi \bar{\Omega}_{sr}^{(1,1)}} 10^{20} \tag{2.37}$$

$$\lambda_{vib,s=m} = \frac{8}{3} k_B C_{V_{vib,s}} \frac{\sqrt{\pi k_B T_c m_s}}{\pi \bar{\Omega}_{sr}^{(1,1)}} 10^{20} \tag{2.38}$$

$$\lambda_{exc,s \neq e} = \frac{8}{3} k_B C_{V_{exc,s}} \frac{\sqrt{\pi k_B T_c m_s}}{\pi \bar{\Omega}_{sr}^{(1,1)}} 10^{20} \tag{2.39}$$

Where μ_s represents the viscosity for one specie *s*, $\lambda_{tra,s}$ is the translational thermal conductivity and $\lambda_{rot,s}$, $\lambda_{vib,s}$ and $\lambda_{exc,s}$ represent the internal energy modes thermal conductivity. So, the total thermal conductivity for a single specie mixture is [13]:

$$\lambda_s = \lambda_{tra,s} + \lambda_{rot,s} + \lambda_{vib,s} + \lambda_{exc,s} \tag{2.40}$$

Ambipolar diffusion

In an ionized gas, another phenomenon to account for is the forced mass diffusion due to the electric field created by the charged particles. This results in increased diffusion of the ions, which are being pulled by the more mobile electrons. Consequently, the electrons will slow down and end up diffusing at the same velocity as the ions. This phenomenon is known as ambipolar diffusion and enforces a quasi-neutral diffusion flux:

$$\sum_s q_s \vec{J_s} = 0 \tag{2.41}$$

with q_s being the charge per unit of mass of the species *s*. Given that the electrostatic forces are not accounted for in the conservation equations, ambipolar corrections should be applied to the diffusion mass fluxes of charged particles.
For ions, the ambipolar diffusion is evaluated as [20].

$$D_{ion}^a = \left(1 + \frac{T_e}{T_{ion}}\right) D_{ion} \tag{2.42}$$

where D_{ion} is the non-corrected diffusion flux of the ion, and T_e and T_{ion} are the translational temperatures of the electrons and ions, respectively. In thermal equilibrium conditions, T_e=T_{ion}, therefore, Equation 2.42 becomes D_{ion}^a = 2D_{ion}.

For electrons, a correction is obtainable by letting the average diffusion of electrons be equal to the average diffusion of ions. Thus, the electron ambipolar diffusion is defined as a weighted sum of the ions ambipolar diffusion [20]:

$$D_e^a = M_e \frac{\sum_{s=ion} D_s^a \, x_s}{\sum_{s=ion} M_s x_s} \tag{2.43}$$

In the case of having only one species present, D_e^a=D_s^a.

Chapter 3

Numerical Setup

This chapter focuses on the numerical implementation of the mathematical and physical models presented in Chapter 2. First, the heat flux correlations are used to select the trajectory points that are going to be tested with the SPARK code. Next, a computational domain description will be presented, discussing the type of vehicle involved and the mesh generation. At last, the CFD numerical solver is presented, and the subsequent simulation parameters and strategy are prepared.

3.1 Trajectory points choice

In order to determine the accuracy of the simulations, we are going to compare the results with the following models for the convective and the radiative heat fluxes.
For the convective heat, the Sutton-Graves relation was applied [9]. It is a general equation for the stagnation point convective heating to an axisymmetric blunt body for gases in chemical equilibrium, formulated as a function of the mass fraction, molecular weight and transport parameter of the base gases.

$$\dot{q}_{conv} = K\sqrt{\frac{\rho}{r_n}}v^3 \tag{3.2}$$

where K is a coefficient derived as a function of the gas mixture, and for Venus is taken as K = 1.8960×10^{-4} , r_n is the nose radius of the vehicle, and v is the freestream velocity.
To analyse radiative heating, it will be used some empirical models based on the Pioneer Venus mission data [21].

$$\dot{q}_{rad} = \begin{cases} 8.497 \cdot 10^{-63} v^{18} \rho^{1.2} r_n^{0.49} & for\ \ 10.028 < v < 12\ km/s \quad (3.3a) \\ 2.195 \cdot 10^{-22} v^{7.9} \rho^{1.2} r_n^{0.49} & for\ \ v < 10.028\ \ km/s \quad (3.3b) \end{cases}$$

As already stated, since the radiative heat is at least one magnitude of order smaller than the convective heat flux, the purpose of this work is to concentrate on the heat fluxes predicted by Sutton-Graves.
In Figure 3.1 the convective and the radiative heat fluxes are presented along with the time of the flight and the altitude.

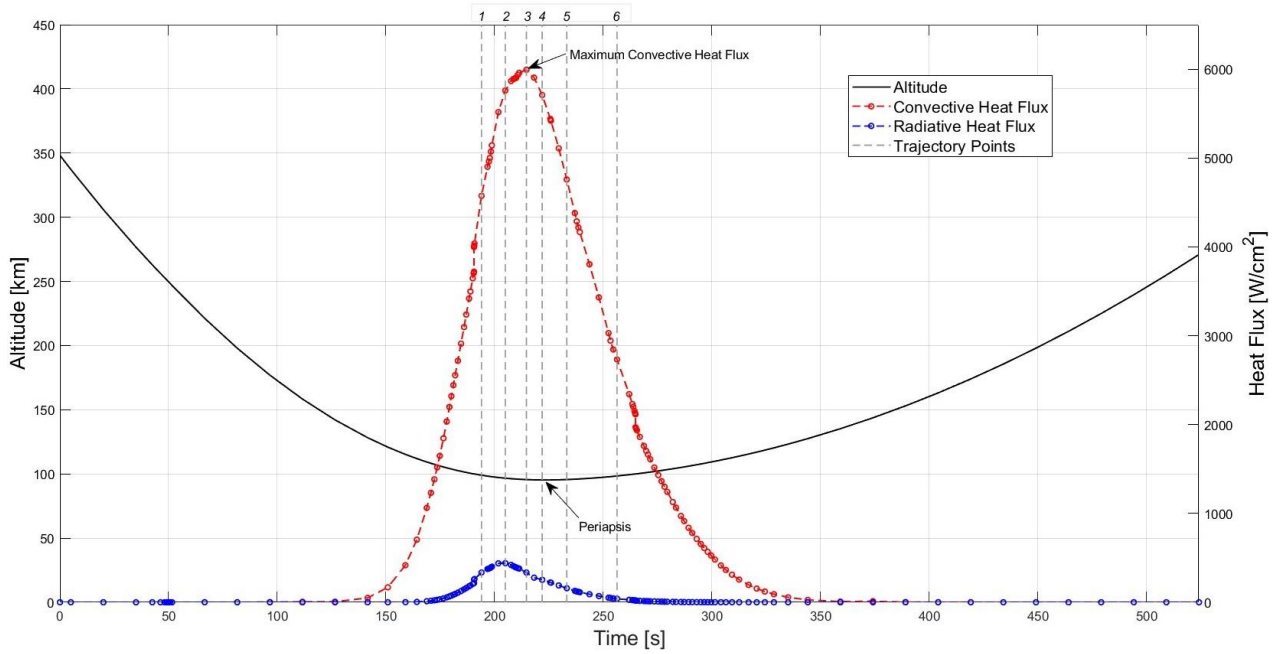

Fig 3.1.: *In this figure we can see the trend of both the heat fluxes along the time and the altitude. It's clear that the convective heat flux much higher than the radiative heat, so that can be negligible.*

The trajectory data has been calculated by the mission analyst of the CDF work, using the General Mission Analysis Tool (GMAT) of NASA to numerically solve the equations of motion with a high grade of accuracy [22].
Six points were selected to perform the simulations. The most critical, point 3, corresponds to the peak of the convective heat flux. Another interesting point to have been tested is the periapsis, that correspond to the fourth point. Points 1 and 6 are chosen in order to have them in the threshold of the continuum regime and points 2 and 5 are taken in between. Table 3.1 show the selected points data for the trajectory.

Points	Altitude [km]	$\boldsymbol{u}_\infty$ [km/s]	$\boldsymbol{p}_\infty$ [Pa]	$\boldsymbol{T}_\infty$ [K]	$\boldsymbol{\rho}_\infty$ [kg/m^{-3}]	$\boldsymbol{K_n}$
1	98.9966	10.8012	3.5250	166.9474	1.0998×10^{-4}	9.69×10^{-4}
2	96.6627	10.5246	6.3196	170.1277	2.0372×10^{-4}	5.59×10^{-4}
3	95.5855	10.1710	8.3968	168.7856	2.7076×10^{-4}	4.12×10^{-4}
4	95.3109	9.8726	9.0342	168.5109	2.9374×10^{-4}	3.86×10^{-4}
5	95.6298	9.4393	8.2983	168.8301	2.6706×10^{-4}	4.16×10^{-4}
6	98.4098	8.8841	4.0434	169.9220	1.2671×10^{-4}	8.55×10^{-4}

Tab 3.1: *The values of the upstream flow for different points tested are presented in this tab.*

When selecting the free-stream conditions for the CFD simulations, a special attention needs to be given to the limits of the physical models employed in the numerical code. The Knudsen number is a relevant dimensionless value that gives a numerical account of whether the continuum hypothesis can be applied. It is also of particular interest when assessing the *no-slip boundary condition,* in which the flow directly in contact to the wall is assumed not to move [23]. The conventional viscous flow no-slip conditions begin to fail at a certain altitude, depending on the body geometry. The value that is commonly taken as the threshold so that continuum flow and the no-slip condition can be considered is equal to 10^{-3} [24]. As these slip

effects start taking place, the governing equations of the flow are still assumed to be the usual continuum-flow equations, apart from the proper velocity and temperature-slip conditions employed as boundary conditions. As the altitude increase, and the atmosphere of the planet become thinner, the continuum-flow equations are no longer valid and, in order to predict the aerodynamic behaviour, methods from kinetic theory must be used. The threshold after which we consider the flow no-continuum is 10^{-1} and statistical methods are needed to be used for characterizing the behaviour of the gas [25].

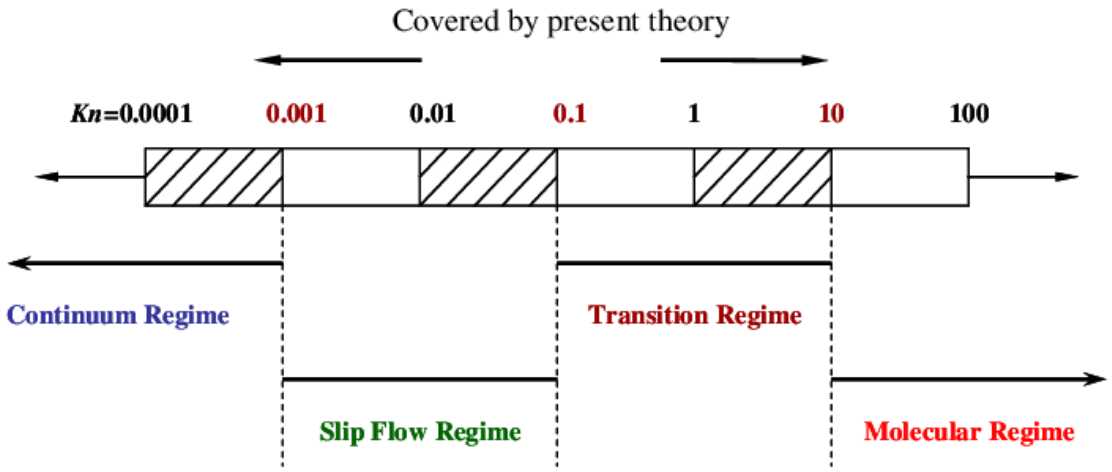

Fig 3.2: *Classification of the flow regimes with Knudsen number.*

The Knudsen number is obtained by the following expression:

$$K_n = \frac{k_B T_\infty}{\sqrt{2}\pi d^2 p_\infty l} \tag{3.4}$$

Where k_B is the Boltzmann constant, T_∞ is the thermodynamic temperature of the upstream flow, p_∞ is the total pressure of it, d is the hard-shell diameter of the particle and l is the characteristic length of the probe. We can calculate it as the actual length of the sphere-cone. As the Tab 3.1 shows, the Knudsen number is K_n < 0.001, so the flow will be in continuum regime. It is concluded then that the use of the Navier-Stokes equations with no slip boundary condition is valid, and that SPARK can properly model the behaviour of the flow.

3.2 Computational domain

In order to perform the described simulations, the use of a suitable mesh is required. In this case the 45° sphere-cone has been chosen as it has been used in various past successful missions as Pioneer on Venus itself, Hayabusa re-entry probe or Galileo mission. As already specified the capsule used for these simulations is the smaller vehicle of the Pioneer mission, with a nose radius of 0.3 metres and a base radius of 0.3365 [19].

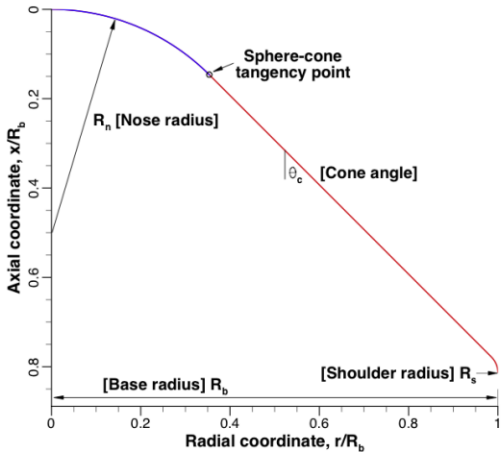

Fig 3.3: *Geometry of a 45° sphere-cone* [26].

The body is axisymmetric and therefore, only half of the front body will be considered in the computational domain. The domain is discretized into a single-block mesh of $N_i \times N_j$ cells, where N_i is the number of cells in the normal direction, along the stagnation line, and N_j is the number of cells in the tangential direction, along the vehicle's surface.

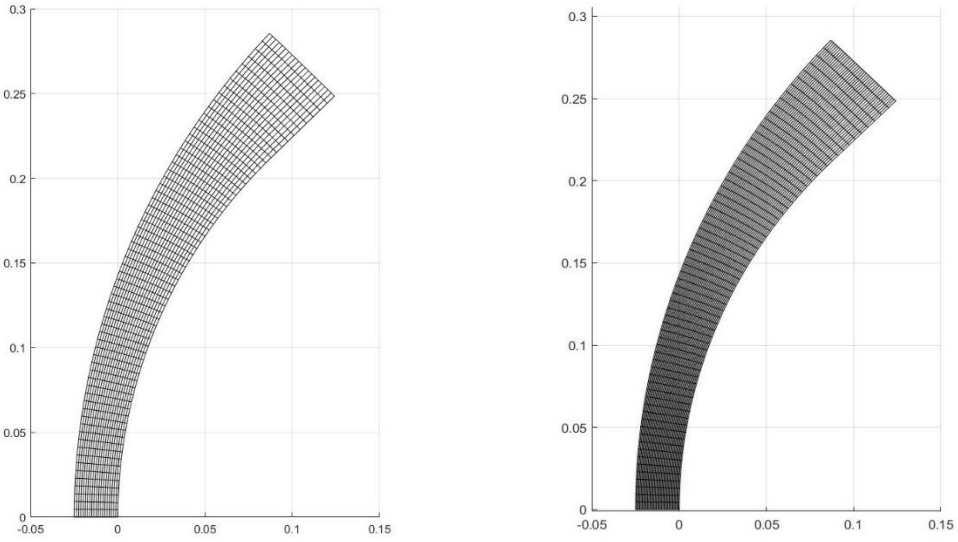

(a) 20 x 65 mesh. (b) 40 x 65 mesh.

Fig 3.4: *examples of structured meshes generated for the simulation*

After a convergence analysis it was found that a mesh with $N_i = 40$ cells is the best compromise between precision and computational cost. The number of cells in the tangential direction of the vehicle doesn't have a significant influence on the results, so the mesh used for this work will be the (b) in the example above.

3.2.1 Refinement at the shock and at the boundary layer

Another important aspect taken in consideration is the refinement of the mesh at the shock and at the wall. The fine-tuning at the shock and the boundary layer is done by finding abrupt changes in the temperature and pressure fields of a previously computed solution. This search routine is performed inside SPARK where the mesh is clustered at the critical regions. The

refined mesh is represented in Figure 3.5 where the shock wave and the boundary layer are both clustered.

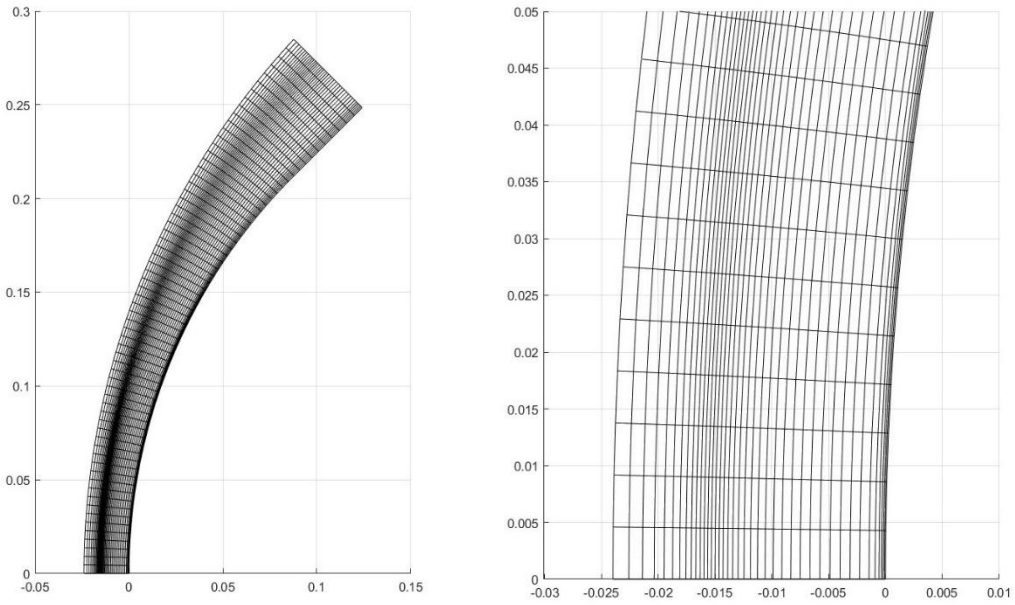

Fig 3.5: *The mesh after the adaptation. On the left the full mesh is presented, while on the right a zoom at the stagnation line is shown.*

The fine-tuned mesh allows a further improvement on the solution, especially at the boundary layer, where now the denser mesh fully captures the steep gradients at the vehicle's wall. The boundary layer was refined up to a wall Reynolds number Re_w = 10 in the boundary layer frontier cells and a shock clustering set at 2.5. More refinement was not reasonable as this would have decreased the time step beyond reasonable values. In this work the stagnation line temperature does not have a very well defined peak in the shock layer. It doesn't represent a problem for the purpose of this work since the convective heat fluxes will not depend on the shock-layer peak, but only on the boundary layer refinement.
In the figure 3.6 it is shown how the mesh adaptation affects the trend of the temperature along the stagnation line.

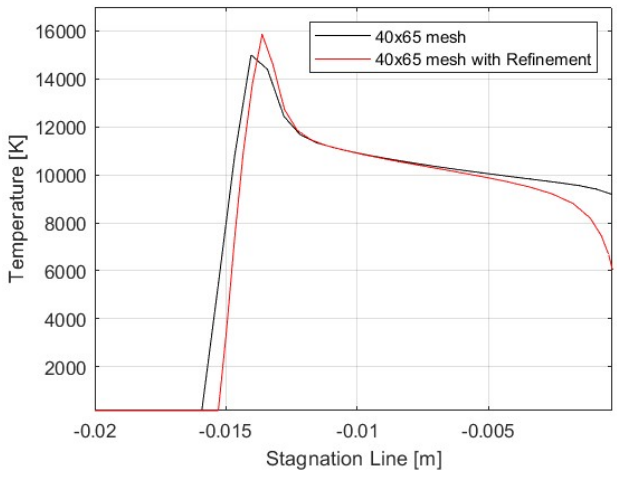

Fig 3.6: *Temperature trend at the stagnation line for both a simple and a refined mesh*

3.2.2 Boundary conditions and Catalycity

Figure 3.7 illustrates the boundary conditions applied to the computational domain. The upstream inflow conditions are defined in Table 3.1 for each trajectory point.
Heating to hypersonic vehicles during flight is not only governed by the state of the flow around the vehicle, but also by the chemical or species boundary conditions. The surface may chemically react with the flow surrounding the vehicle, that is, the surface may be consumed or transformed (ablation). However, it is out of the scope of this work to consider a surface that undergoes chemical changes [27].
At the outflow, a supersonic outlet boundary condition is imposed, where the conditions at the boundary are extrapolated from the interior domain. A symmetry boundary condition is set at the stagnation line, which mirrors the solution without allowing any fluxes to cross it. And finally, a catalytic and isothermal boundary condition is imposed at the vehicle's wall.

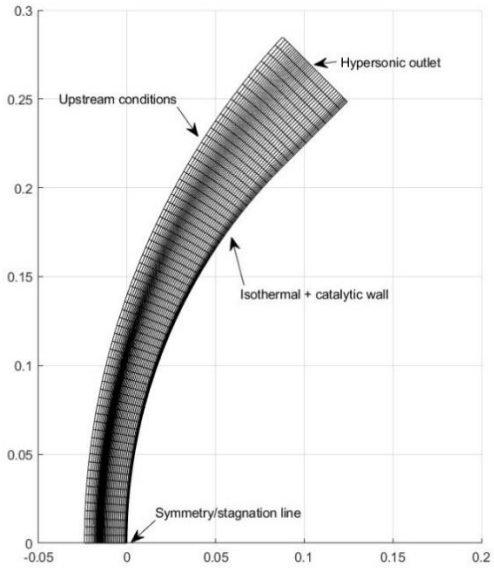

Fig 3.7: *Boundary conditions applied to the computational domain.*

When atoms hit the surface of a material, they may react to form molecules while releasing some or all their heat of dissociation. Catalycity is a macroscopic parameter to describe surface catalysis, the capability of a material to enhance a chemical reaction rate or change its equilibrium constant. It is usually called a material property, due to its strong dependence on the surface material. We can define the wall as:

- Non-catalytic: no atom/ion recombination resulting in the wall not being affected by the flow.
- Partially catalytic: There is some atom/ion recombination.
- Fully catalytic: Full atom/ion recombination.

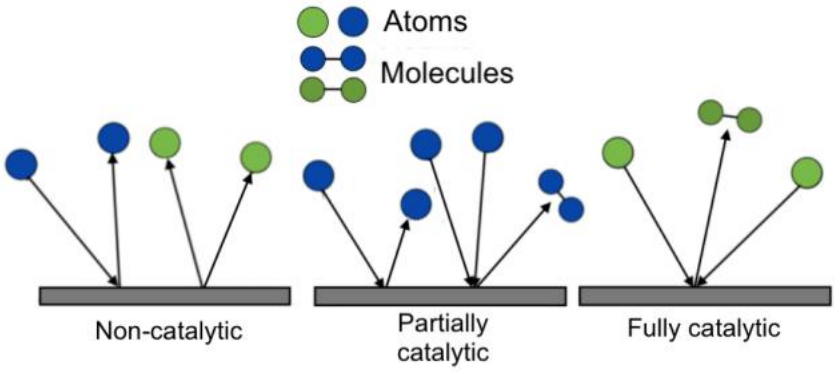

Fig 3.8: *The effect of wall catalysis on atom recombination.*

The fully catalytic option is the one that maximizes the wall heating, since the recombination process is an exothermic reaction, and thus, it is the one that will be adopted in this work in a conservative fashion.
The wall boundary is set to be fully catalytic and kept at a constant temperature (Isothermal wall) assumed to be T_w = 1200 K, owing to the radiative equilibrium wall temperatures predicted by the analytic method (1,400-1,600K). The wall temperature was slightly decreased in anticipation for the lower calculated wall heat fluxes [18].

3.3 CFD Solver

SPARK, the *Software Package for Aerothermodynamics, Radiation and Kinetics*, is the CFD code used to simulate multi-dimensional hypersonic flow, developed at the University of Illinois and by the Instituto de Plasmas e Fusão Nuclear and that is the only Aerothermodynamic tool available in Portugal [28]. Unlike many other software for CFD simulations, SPARK can implement different physical models and numerical techniques in a unified framework that shares the same data structure, offering more flexibility and extendibility. The exceptional multi-physics nature of the hypersonic flow determines the importance of the design characteristic of this software. The code can work with Euler equations or Navier-Stokes compressible flow equations. The simulations are available in 0D (that are temporal independent), 1D (post-shock relaxation) or 2D (cylindrical or axisymmetric). The SPARK is coded in Fortran 03/08 taking advantage of object-oriented programming techniques and high computational efficiency. Treating each physical quantity and physical model as an object that enables the separation of different physical models, numerical methods and mesh-related operations. Mesh grids can be generated using an external software. In this work the MATLAB software is used for this scope.
The SPARK code can use both a multi-temperature or a state-to-state approach, which allows to simulate the typical non-equilibrium conditions experienced at high altitudes during an atmosphere fly-by or a re-entry. The gas models available are: perfect gas condition, frozen gas or chemically reacting non-equilibrium gas mixture that involve chemical kinetic models. Catalytic effects can also be simulated at the wall, but this option is still not fully available. It provides also a mesh refinement tools for shock and/or boundary layer capturing. There are also two types of time discretisation, implicit or explicit. There is no possibility to model turbulence in the code and, therefore, the flow is assumed to be laminar all along the body [29].

3.4 Simulation Input

In order to launch SPARK and run the simulations, a key word-based input file must be provided with
the initialisation parameters. The file structure is presented in this section:

```
Start(Spark)
```

- Here is defined how verbose will be the spark.log

```
  Start(Logger)
   LogLevel = 100
  End(Logger)
```

- Here is defined the results directory and the database directory:

```
Start(Environment)
    UserDirectory = ./dtb
    WorkingDirectory = ./Spark Results
End(Environment)
```

- Here is defined with what frequency a restart file is written. In this case, every 10000 iterations and for a maximum of 3 restart files. The restart file is useful to make a simulation from a previous solution and not from scratch. This strategy was helpful to get better results and the adaptation of the mesh around the wall and the shock wave.

```
Start(Output)
    RestartFile( File=spark.rst, IterFreq=10000, MaxFiles=3)
End(Output)
```

- Here the mesh geometry and the boundary conditions are defined.

```
Start(Mesh)
    Mesh = File("mesh.msh")
    Start(Processing)
       Plot(File="meshBound.pdf", ShowBoundaries=T)
       Plot(File="meshNodes.pdf", ShowNodesLabel=T)
    End(Processing)
End(Mesh)

Start(BoundaryConditions)
   Upstream(iMin)
   Wall(iMax, Tw=1200) #Isothermal wall at 1200 K
   Symmetry(jMin)
   SupersonicOutlet(jMax)
End(BoundaryConditions)
```

- Here the simulation type is defined. In this work will work with a 2D axisymmetric case.

```
Start(Simulation)
     Simulation_Type = 2D_AXI
End(Simulation)
```

- Here the solver parameters and stopping criteria for the calculation are defined. Time discretization is a mathematical technique that involves the integration of every term in different equations over a time step. In SPARK it's possible to have both Implicit and Explicit time integration methods.
  Another important value is the cfl, a non-dimensional number that evaluate the time step requirements of a transient simulation for a given mesh size and flow velocity, linked to the Courant-Friedrichs-Lewy condition. The way these parameters are set during the simulation will be explained in the following section about the strategy that has been developed in this work.

```
Start(Solver)
     Time_discretization = Implicit/Explicit
     Convective_Scheme   = Harten_Ye
     Scheme_order        = 2
     StopCondition(Iter=200000, Residual=1e-4)
     cfl(0.01)
End(Solver)
```

- Here the gas state is defined, which is the gas model, the type of the flow, the detailed composition and chemistry of the flow and the upstream conditions of it. In this work a kinetic model of 19 species and 36 reactions will be used for the simulations. The chemistry will be simpler than that, there will be no nitrogen and correlated species.

```
Start(Gas)
     Gas_Model = Frozen_Gas/Nonequ_Gas
     Flow_Type = Euler/Navier_Stokes
     Kinetic = CO2_N2-19spe-36rea
     Species = CO2, O2, CO, C, O, O2+, CO+, C+, O+, e-
     Upstream = State(P=9.034170461, T=168.5108702, M=48.15469676,
     Xi="CO2:1")
End(Gas)
```

- Here the thermodynamic model is defined. For this work only the polynomial one is used.

```
Start(Thermodynamic)
     Thermodynamic_Model        = Polynomial
     Polynomial_model           = NASA9
End(Thermodynamic)
```

- Here the transport model is defined. In SPARK the Gupta and Wilke models are available:

```
Start(Transport)
    Transport_Model = Wilke/Gupta
End(Transport)
```

3.6 Simulation Strategy

Hypersonic flows, alongside turbulent flows, represent some of the most challenging and unforgiving problems in contemporary CFD applications. Compared to a re-entry, an entry flow at a velocity of 10 km/s present some convergence issues. In this section, the strategy to face with these problems is discussed.

Frozen vs. Non-equilibrium: The frozen gas assumption implies that there is no chemical activity nor energy exchange processes occurring in the gas, i.e. there are no kinetic and energetic source terms to the mass and energy conservation equations. The chemical non-equilibrium is described by the chemistry model section. The thermal non-equilibrium is described in the multitemperature section. Since this section is not available in SPARK at the moment of this work, we consider thermal equilibrium for all the simulations. This approximation can be accepted since the convective heat fluxes are way higher than the radiative heat fluxes.

Wilke vs. Gupta-Yos: In this work only the Wilke transport model will be tested.

Implicit vs. Explicit: the best way to get a convergence is to consider an implicit time discretization. This method is not always used due to the computational effort required, since the explicit method is faster. It is indeed the most stabile between the two and the one that gave the better results.

Euler vs. Navier-Stokes: The Euler flow model set an inviscid flow in which transport phenomena are neglected (diffusion, viscosity and thermal conductivity). The Navier-Stokes flow type is applied in order to consider the boundary layer near the surface of the capsule.

The simulations were started in Euler without the chemistry (frozen flow), to allow for the shockwave to stabilize, and then restarted considering chemical non-equilibrium model and Navier-Stokes flow type. After that, another restart in order to have a mesh adaptation was done. The simulations were run in implicit, with low CFL numbers, owing to the strong numerical fluxes induced by the strong shockwave.

Chapter 4

Results

The CFD results are presented in this chapter. First, the impact of the flowfield models on the results is discussed in Section 4.1. Then, a detailed analysis of the results for the peak trajectory point is presented in Section 4.2, both for the stagnation line and the 2D flowfield. Finally, in Section 4.3 the heat fluxes on the spacecraft will be discussed.

4.1 Impact of the Flowfield Models

Impact of the Gas Models

The frozen flow is characterized as having a zero-reaction rate, implying that its chemical composition is constant throughout space and time. Although not a very realistic model, it is computationally faster than the non-equilibrium gas model, which allows faster preliminary computations, such as the ones for mesh assessment.
Figure 4.1a shows the difference in temperature between the two models for the key trajectory point 3 in a simple mesh (without the refinement). The frozen flow is composed of 100% CO_2 for the entire process, meaning no dissociation or ionization occurs. All the thermal energy is contained within this specie without allowing the endothermic reactions of ionization and dissociation that could lower the temperature after the shock wave. This assumption leads to a thicker, higher temperature shock layer. The temperature remains constant for the entire shock layer until reaching the thermal boundary layer, where it decreases due to the imposed wall temperature. Figure 4.1b shows that the pressure jump is roughly the same for both models.

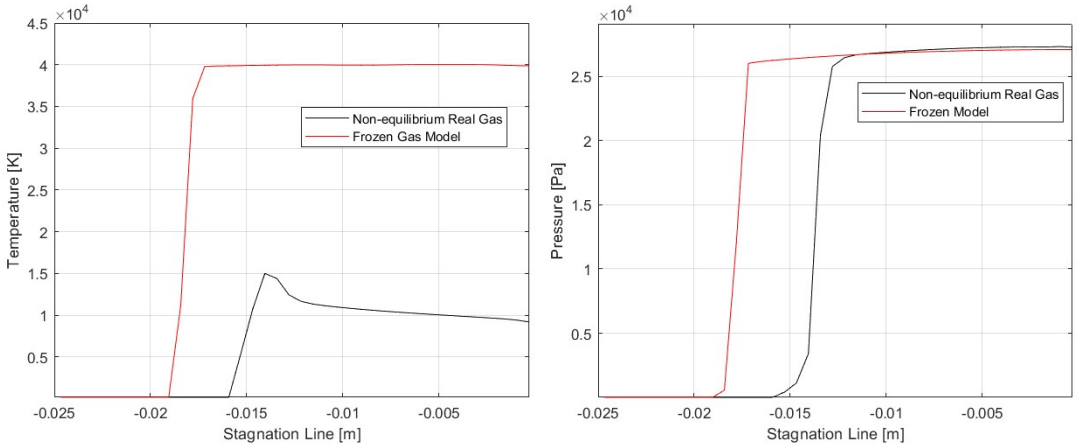

(a) Temperature profiles. (b) Pressure profiles.

Fig 4.1: *Stagnation line comparison between frozen gas and non-equilibrium gas.*

Impact of the Chemical Models

To verify the impact of the number of species, two models were studied: the 10-species model and the 5-species model. The 10-species model is composed by the following species: CO_2, O_2, CO, C, O, O_2^+, CO^+, C^+, O^+, e^-. The 5-species model considers only the neutral species without the ions: CO_2, O_2, CO, C, O.
In the following Figure it is shown that the two model have some differences if we focus on the neutral species. The CO_2 dissociation is more intense for the 5 species model: this is because the simplest chemistry brings a stronger shock. In fact, the high velocities considered in this work allow enough ionization to generate these differences in the results.
The recombination of the CO_2 and O_2 molecules is compensated by the decrease of the C and O species in the neutral species only, while in the 10 species model it is shown how this compensation is made by the decrease of the ions and electrons too.

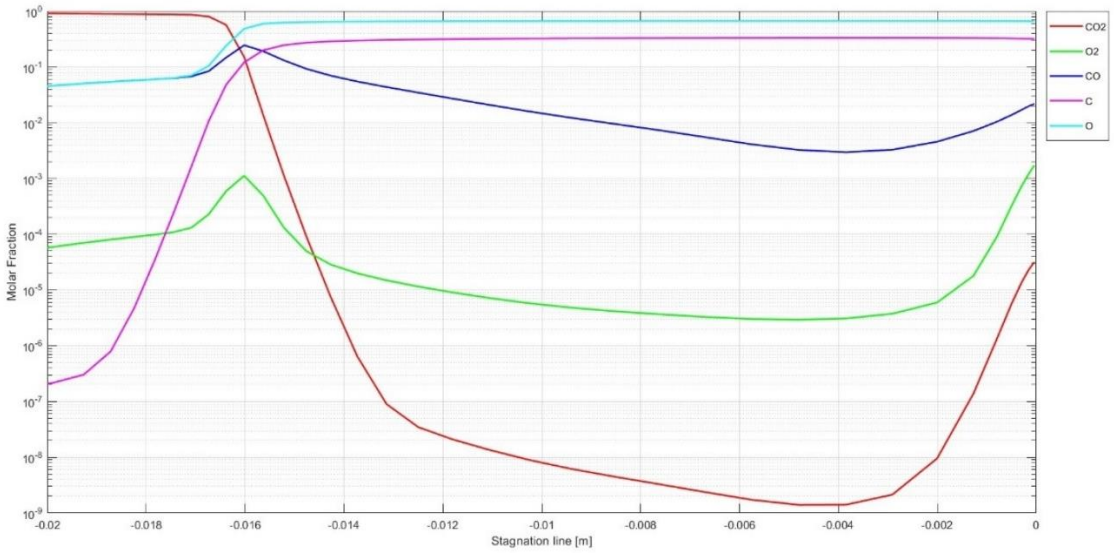

(a) 5-species model molar fractions.

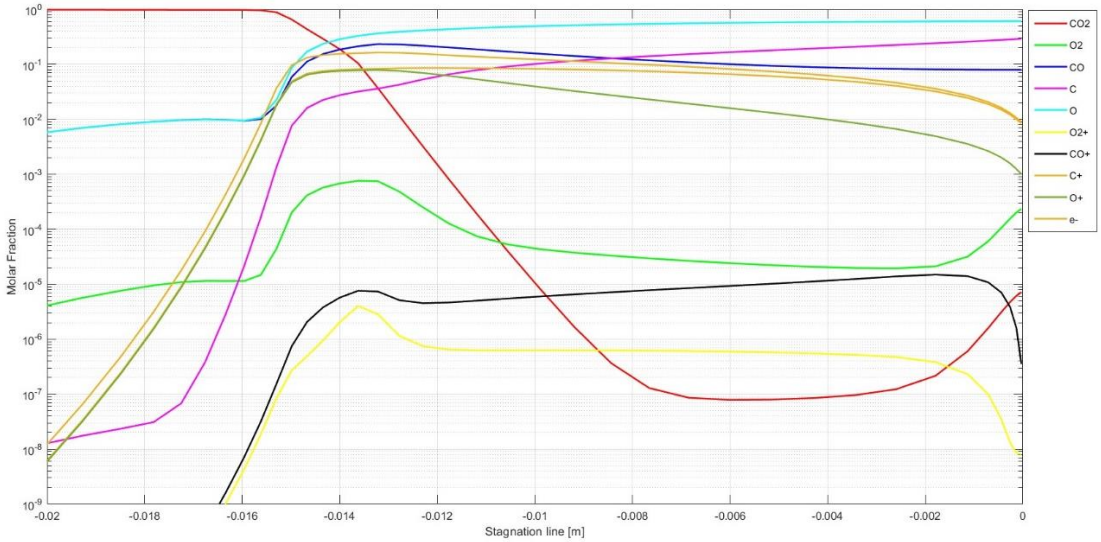

(b) 10-species model molar fractions.

Fig. 4.2: *Molar fractions for the different chemical models.*

A comparison between the calculated heat fluxes using the 5 species model only, and the more detailed 10 species model is presented in Figure 4.3. Considering only the neutral species overestimate the heat fluxes as it is pictured.

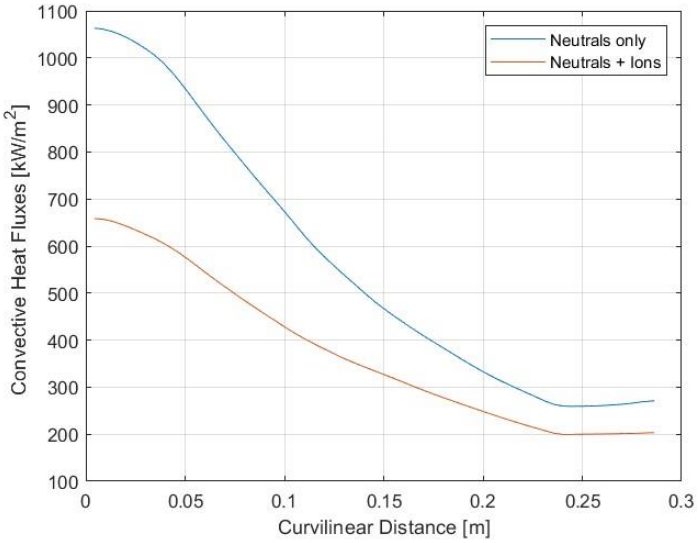

Fig. 4.3: *Wall heat fluxes comparison for both the models*.

4.2 Peak Heating Trajectory Point Analysis

A detailed analysis of the results at the peak heating trajectory point is presented here. These results are further discussed in Section 4.3.

4.2.1 Stagnation Line Analysis

The most substantial high-temperature effects occur at the stagnation-point of the vehicle, so the analysis of the stagnation line requires particular consideration. Figure 4.4 describes the sudden changes in the flow properties along the stagnation line. At the shock wave, $x = -1.5 \times 10^{-3}$ m, the pressure abruptly increases 3000 times to roughly 270 kPa, and the particle velocity drops one order of magnitude. The kinetic energy of the flow is transformed into thermal energy, causing the shock wave to reach temperatures up to 15800 K, which is sufficiently high to promote dissociation and some ionization of the species present in the flow. Afterward, at the vehicle's wall, the heat convects to the vehicle surface while the high-density boundary layer and the catalytic wall promote recombination between the species.

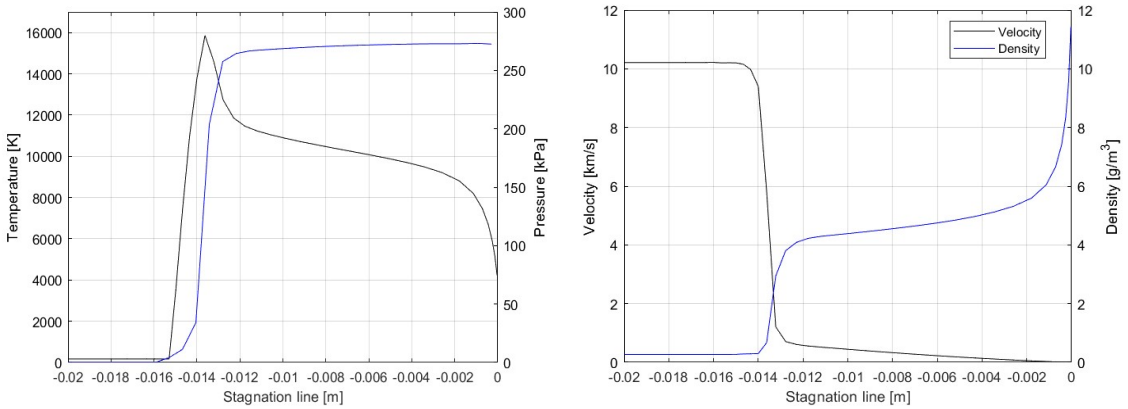

(a) Temperature and pressure

(b) Density and velocity

Fig 4.4: *Stagnation line profiles for temperature, pressure, velocity, and density.*

The species' molar fraction along the stagnation line is shown in Figure 4.2b. Before the shock wave, the flow is composed only of diatomic carbon dioxide. As the fluid approaches the shock wave, the concentration of some species may increase slightly due to mass diffusion, which is not constrained by the shock wave. Across the shock, as dissociation and ionization occur, the molar fraction of CO_2 decrease and give rise to CO, O_2, O and C. Ionized species and free electrons also start to increasingly populate the gas mixture, although in small concentrations. Eventually, the chemical composition stabilizes, remaining constant until reaching the boundary layer.

When the particles reach the dense boundary layer and the catalytic surface, some recombinations take place, increasing the population of the molecular species, CO_2 and O_2, at the expanse of CO and charged species.

4.2.2 2D Flowfield Analysis

After the simulation was completed, the code is able to plot some 2D figures in which it is shown the behaviour of the flow around the spacecraft.
Figure 4.5a describes the temperature field. At the stagnation point, the normal shock wave induces large temperature gradients, making the shock front very well-defined. Then, as the flow moves along the spherical nose, the shock starts weakening since it becomes oblique to the freestream velocity, which allows a gradual decrease in the temperature.
The pressure distribution in Figure 4.6b clearly shows the pressure build-up at the nose region and how it attenuates along the nose tangential direction.

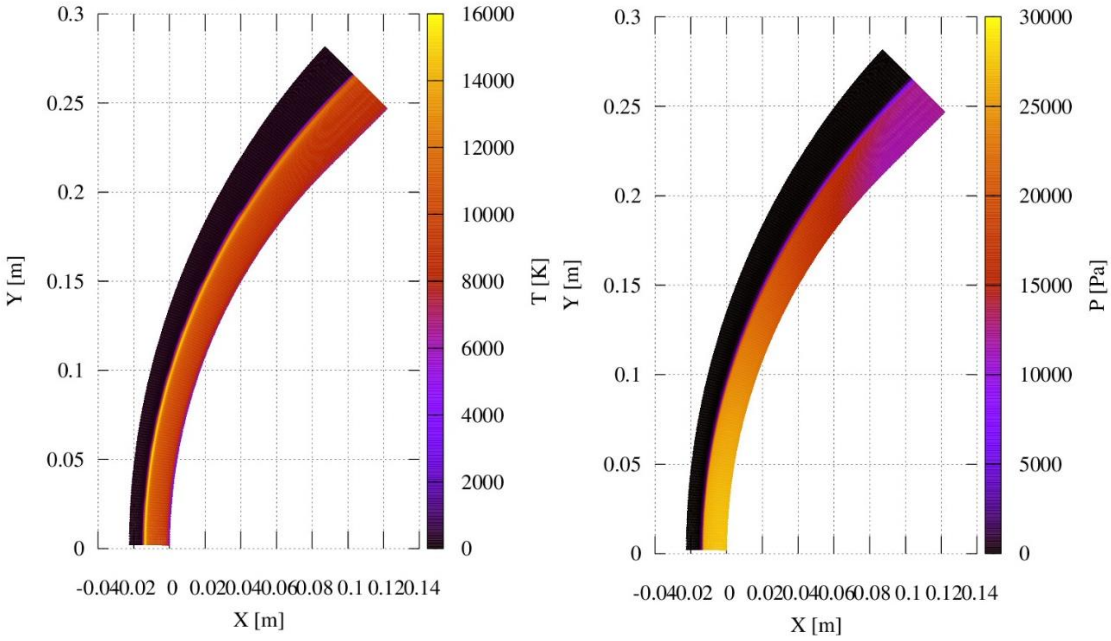

(a) 2D temperature profile

(b) 2D pressure profile

Fig. 4.5: *Temperature and Pressure profile for the 2D flowfield.*

Figure 4.6 depicts some examples of the chemistry within the 2D flowfield as a way to illustrate the general behaviour of the chemical species present in the flow. In the figure 4.6a it is shown how the upstream flow is dominated only by CO_2. Right after the shock the neutral species are visible, while the ions start to appear. In this figure it is clear how the charged particles are focused especially around the nose of the spacecraft, due to the higher temperature of this region, and how they decay near the wall due to the imposed wall temperature, giving space to the recombination of the neutral species.

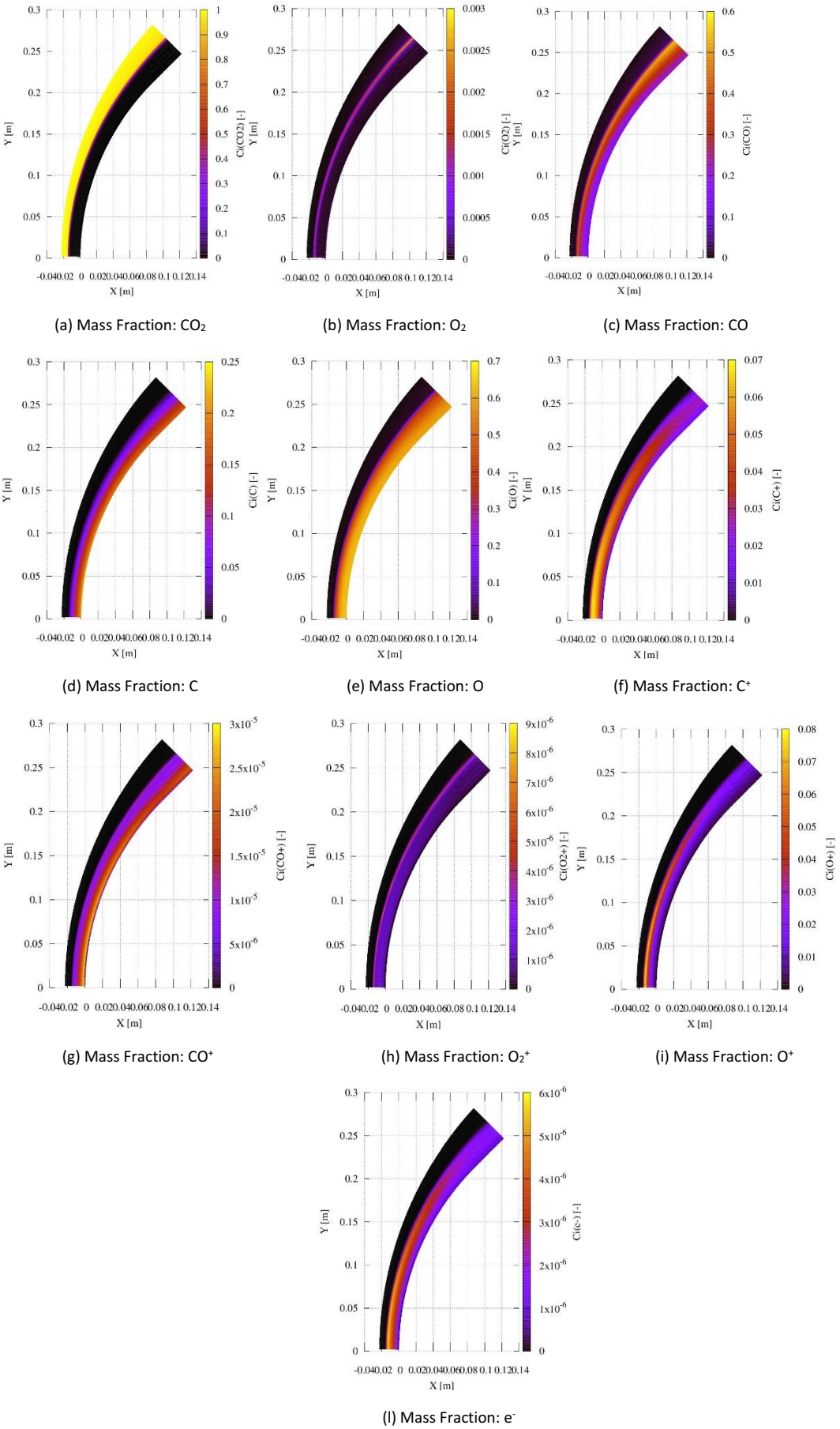

(a) Mass Fraction: CO_2 (b) Mass Fraction: O_2 (c) Mass Fraction: CO

(d) Mass Fraction: C (e) Mass Fraction: O (f) Mass Fraction: C^+

(g) Mass Fraction: CO^+ (h) Mass Fraction: O_2^+ (i) Mass Fraction: O^+

(l) Mass Fraction: e^-

Fig. 4.6: *Mass fraction profiles of the different species along the body in the 2D flowfield.*

4.3 Wall Heating

The CFD simulations for the six trajectory points allow the computations of the heat fluxes at the wall. Figure 4.7 shows the heat fluxes along the spacecraft's wall. Note that the heat flux is maximum at the stagnation point, where it reaches 658 kW/m^2 for the trajectory point 3. Then, it decreases steeply along the tangential direction of the nose until stabilizing at 200 kW/m^2 when it reaches the conical section.

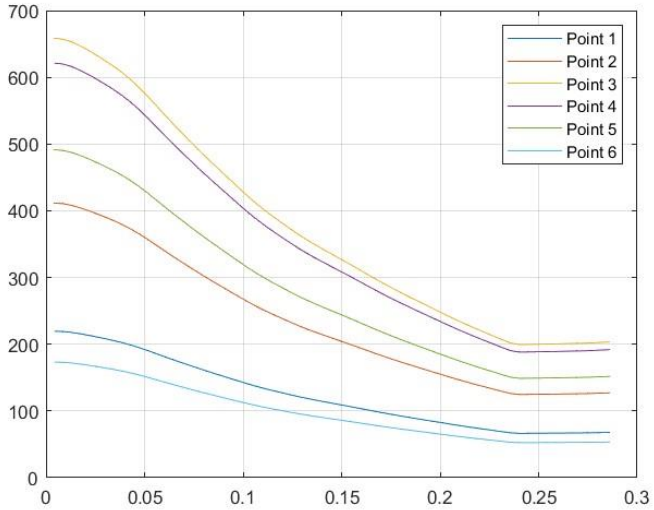

Fig. 4.7: *Heat flux CFD results for the six trajectory points.*

The empirical correlations were used beyond their limitations as a practical way to estimate at which segment of the trajectory the peak heating is maximum. The Sutton-Graves correlation overpredicted the values of the heat fluxes of one order of magnitude. This is due to the fact that the correlation is valid for bigger spacecrafts than the one used in this work, with a nose radius of only 0.3 metres. Nevertheless, the correlations predicted reasonably well where the peak heating occurs, allowing to choose the six trajectory points that describe the heating profile during the atmospheric entry.

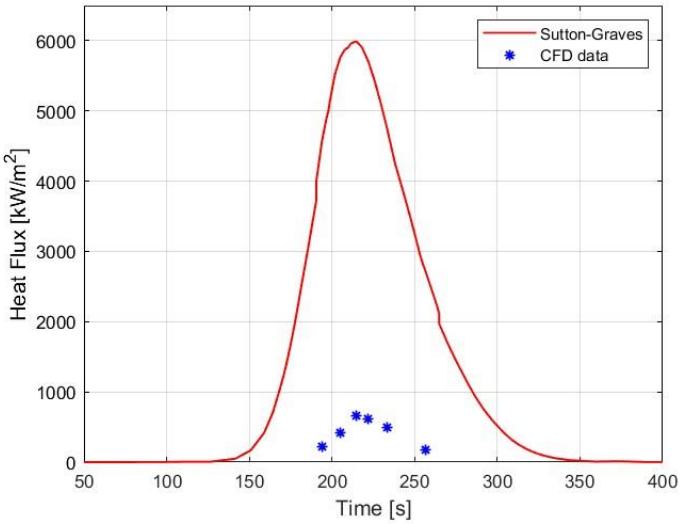

Fig. 4.8: *Comparison between the Sutton-Graves correlation and the CFD results for the heat fluxes.*

Chapter 5

Conclusions

5.1 Achievements

In this work, a CFD aerothermal analysis of the peak heating trajectory point was performed, assessing the physical and chemical characteristics of the flow within the shock layer. Furthermore, the heat fluxes along the vehicle's wall were successfully computed for other trajectory points, which, in the future, may contribute to develop an empirical model and to design a suitable thermal protection system.
An empirical correlation was tested beyond their limitations for predicting the convective heat flux along the trajectory. The CFD computations reasserted that the Sutton-Graves correlation is unsuitable for small entry vehicles. The correlation overpredicted the heat fluxes by nearly one order of magnitude. The correlation is inversely proportional to the nose radius, so for smaller nose radii the solution becomes highly non-linear and quickly rises up. Nevertheless, it captures the overall trendline of the heat fluxes quite well, which allowed to estimate the relevant trajectory points for the CFD aerothermal analysis.
A comparison between the different chemical models demonstrated that for superorbital velocities, where the ionization of the particles is intense, the gas can be better modelled with neutral plus ions species – the so-called 10-species model.

5.2 Future Work

Based on the results obtained in this work, a few recommendations for future development are presented here.

- To complete aerodynamic characterization of the vehicle, including the control and stability derivatives for hypersonic flight.
- To research in the literature other heat fluxes correlations that fit better with this case.
- Evaluate the heat fluxes with a more detailed chemical model that take account of the small amount of N_2 in the Venus atmosphere, and so the correlated reactions of dissociation and ionization involved in it, for example a 19-species chemical model.
- A suitable TPS can be designed given the heat fluxes and heat loads computed in this work. The TPS for such small vehicles may require novel lightweight materials capable of withstanding the severe heating environment experienced during the atmospheric entry.
- To design an effective aerodynamic control system for the vehicle, including trim tabs and body flaps, allowing a controlled and lifting entry trajectory.

Bibliography

[1] M. Bandecchi, B. Melton, and F. Ongaro, Concurrent engineering applied to space mission assessment, 1999.

[2] B. Fegley, Atmospheric Evolution, Venus., Encyclopedia of Earth Sciences Series, 2004.

[3] R. C. Ghail, M. S. Gilmore, S. E. Smrekar, A. H. Treiman, and C. F. Wilson., The exploration of Venus: current understanding and open questions., 2019.

[4] D. Titov, N. Ignatiev, K. McGouldrick, V. Wilquet, and C. Wilson.;, «Clouds and hazes of venus.,» Space Science Reviews, 2018.

[5] Y. Marcq, C. D. Yung, and K. L. Parkinson., «Atmospheric chemistry on venus: an overiview of unresolved issues.,» in *50th Lunar and Planetary Science Conference*, 2019.

[6] J. S. Greaves, A. Richards, W. Bains, P. B. Rimmer, D. L. Clements, S. Seager, J. J. Petkowski, «Phosphine gas in the cloud decks of venus.,» Nature Astronomy, 2020.

[7] J. D. Anderson Jr., in *Hypersonic and High-Temperature Gas Dynamics*, McGraw-Hill Book Compani, 1989.

[8] J. Bertin, Hypersonic Aerothermodynamics, Washington D.C.: American Institute of Aeronautics and Astronautics, 1994.

[9] M. F. P. Bruxelas, «CFD Simulations of Superorbital Reentry for a Phobos Sample Return Capsule,» Master's thesis, Instituto Superior Tecnico, Lisbona, 2017.

[10] L. S. Fernandes, B. Lopez, and M. Lino da Silva., «Computational fluid radiative dynamics of the Galileo Jupiter entry,» Phys. Fluids 31, 2019.

[11] D. F. Potter, «Modelling of Radiating Shock Layers for Atmospheric Entry at Earth and Mars,» Phd thesis, University of Queensland, Australia, 2011.

[12] M. L. Jianlong Yang, «Numerical analysis of hypersonic thermochemical non-equilibrium environment for an entry configuration in ionized flow,» Chinese Journal of Aeronautics, Pechino, 2019.

[13] R. N. Gupta, J. M. Yos, R. A. Thompson e K.-P. Lee, «A review of reaction rates and thermodynamic and transport properties for an 11-species air model for chemical and thermal nonequilibrium calculations to 30000 K,» Work of the US Gov. Public Use Permitted., 1990.

[14] D. K. a. M. Mortazavi, «Simulation of Non-equilibrium Hypersonic Shock Wave Boundary,» Piscataway, NJ 08854, 2018.

[15] V. G. A. K. K. V. Yury Dobrova, «Numerical simulation of hypersonic flow with non-equilibrium chemical reactions around sphere,» Elsevier Ltd., 2021.

[16] C. H. K. J. Walter G. Vincenti, Introduction to Physical Gas Dynamics, Malabar, Florida: Robert E. Krieger Publishing Co., Inc., 1965.

[17] R. N. G. J. L. S. Peter A. Gnoffo, «Conservation Equations and Physical Models for Hypersonic Air Flows in Thermal and Chemical Non-equilibrium,» NASA, Scientific and Technical Information Division, Hampton, Virginia, 1989.

[18] M. L. d. Silva, «VENUS AEROCAPTURE CFD SIMULATIONS 60° SPHERE CONE GEOMETRY,» Lisbon, 2020.

[19] C. R. Wilke, «A Viscosity Equation for Gas Mixture,» The Journal of Chemical Physics, Berkeley, California, 1949.

[20] F. F. Chen, «Introduction to Plasma Physics and Controlled Fusion, volume 1. Springer, 2nd edition,,» ISBN 0306413329,9780306413322.

[21] M. E. Tauber, G. E. Palmer, and D. Prabhu, «Stagnation point radiative heating relations for venus entry».

[22] G. Musso, «Concurrent design study: Venus Atmosphere Sample Analysis mission,» Master Thesis, 2022.

[23] Fu, B. Sunden and J., «Heat Transfer in Aerospace Applications,» in *Academic Press, 1st edition*, 2016.

[24] R. K. Agarwal, K.-Y. Yun, and R. Balakrishnan, «Beyond Navier-Stokes: Burnett equations for flows in the continuum-transition regime,» in *Physics of Fluids*, doi: 10.1063/1.1397256, 2001.

[25] B. E. Rapp, Microfluidics: Modeling, Mechanics and Mathematics. A volume in Micro and Nano Technologies, Elsevier, 2016.

[26] Dinesh K. Prabhu et al., Atmospheric Entry Studies for Venus Missions: 45° Sphere-Cone Rigid Aeroshells and Ballistic Entries, 2013.

[27] J. B. J. J. Bertin, J. Periaux, Advances in Hypersonics —— Wall Recombination and Boundary Conditions in Nonequilibrium Hypersonic Flows - with Applications, doi: 10.1007/978-1-4612-0371-1 6., 1992.

[28] I. d. P. e. F. N. (2016), « Hypersonic Plasmas Laboratory, SPARK,» 2016.

[29] D. A. Andrienko, «Non-equilibrium Models for High Temperature Gas Flows,» Wright State University, 2014.